PP17: Evaluation of DMAPS sensors

Candidate number: 1017490
Supervisor: Professor Daniela Bortoletto

Abstract

Write the abstract at the end.

Contents

1 Introduction

Particle detectors are essential tools in a wide range of physics experiments. They detect particles that the human eye is unable to see, and can operate in environments that are otherwise inaccessible to humans. They also have numerous applications outside of physics, such as diagnostic tools in the medical field, or suitcase scanners at airports. The working principles of a detector require knowledge of multiple areas in physics, including condensed matter physics, nuclear physics, electromagnetism and electronics. No detector is perfect, and it is important to determine advantages and disadvantages of certain detector designs in order to adapt to the environment in which they are used.

In High Energy Physics (HEP), most experiments involve colliding particles. The Large Hadron Collider (LHC)[] at CERN is currently the highest energy accelerator, reaching a design energy of 14 TeV. The interactions occuring during the collisions are studied by reconstructing and identifying the tracks of the outgoing particles using particle detectors. Different types of particle detectors measure different properties. In particular, near the collision point, the tracker detector must reconstruct each outgoing particle and determine where it originates from. Up until now, each LHC event has contained hundreds of tracks. Tracker detectors must therefore have high spatial resolution in order to resolve particles with very close trajectories. Ideally, the particle tracks should not be deflected by the tracker detectors, and it is therefore desirable to reduce the amount of material that the particles have to travel through. Furthermore, the high collision rate at the LHC, 40 MHz[], also require the detectors to have high time resolution and be radiation resistant.

Silicon pixel detectors have many of the properties required by a tracker detector. The current Inner Tracker in the ATLAS detector are 250 μm thin and can achieve as resolution up to 12 μm. Since the start of the LHC, AT-LAS har performed above expectations, resulting in the discovery of the Higgs boson in 2012. However, with the start of High Luminosity LHC in 2026, the demand for cheap, high resolution pixel detectors is higher than before.

In this report, I will report studies of the MiniMALTA, MALTA and MALTA-Cz sensors, which are known as Depleted Monolithic Active Pixel Sensors (DMAPS). DMAPS have superior cost efficiency and require less material, making them suitable for tracker detectors. Until now, DMAPS have not been used in the LHC due to insufficient radiation hardness and timing resolution. However, the ALICE collaboration has recently developed the ALPIDE sensor that meet their criteria for the Inner Tracking System (ITS)[], which operates under less radiation intense environments. Based on this, the MALTA sensor was developed as a radiation hard DMAPS. The MiniMALTA sensor[1] is based on MALTA, but the test board contains 16 monitoring pixels with various modifications that may improve the overall performance. Finally, the MALTA-Cz was recently produced by reprocessing the MALTA on Czochralski silicon substrate, which allows for a larger signal and higher radiation hardness. While the MALTA and MiniMALTA have been studied extensively in test beams at DESY[] and the Diamond Light Source[], some important properties of MALTA-Cz, such as depletion depth, has not been measured yet.

The main objective of this project is to show that the depletion depth of a sensor can be measured accurately using easily accessible radioactive sources, and to estimate the depletion depth of MALTA-Cz. The depletion depth is an important parameter that describe how much of the total silicon thickness contributes to measurement of signals.

2 Working principles of DMAPS

2.1 Charged particles in matter

The main working principle of a particle detector is to generate a signal when a particle passes through the material. A signal is formed when the incident particle deposits some of its energy in the material, mainly due to collisions with electrons. The amount of energy deposited per unit length is described by the

Bethe-Bloch formula[],

$$\Big\langle -\frac{\mathrm{d}E}{\mathrm{d}x} \Big\rangle = K z^2 \frac{Z}{A} \frac{1}{\beta^2} \Big[\frac{1}{2} \ln \Big(\frac{2 m_e c^2 \beta^2 \gamma^2 W_{\max}}{I^2} \Big) - \beta^2 - \frac{\delta(\beta\gamma)}{2} \Big] \tag{1}$$

where $K = 0.307\,075 \,\mathrm{MeV\,mol^{-1}\,cm^2}$, z is the charge of the incident particle, Z is the nuclear charge of the material, A is the mass number of the material, β is the speed in units of c, $\gamma = (1 - \beta^2)^{-1/2}$, $W_{\max}$ is the maximum energy transfer in a single collision and I is the mean excitation energy.

While Eq. (1), which only describe the mean energy loss per unit length, is independent of the thickness of the material, the fluctuations around the mean depend on the material thickness. In particular, the fluctuations follow a Landau distribution[], which has a long tail at higher energies due to rare events of large energy deposits. The most probable energy loss, Δ_p, is given by

$$\Delta_p = \xi \Big[\ln \Big(\frac{2 m_e c^2 \beta^2 \gamma^2}{I} \Big) + \ln \Big(\frac{\xi}{I} \Big) + j - \beta^2 - \delta(\beta\gamma) \Big] \tag{2}$$

Using Eq. (2), the active region of a silicon sensor can therefore be measured.

2.2 Semiconductor physics

Silicon detectors belong a class of detectors known as solid state detectors. Solids are classified as insulators, metals and semiconductors, depending on their physical properties such as electrical conductivity. These properties can be described by studying how the electrons in the solid interact. The electrons in a solid effectively move in a periodic lattice, and the energy eigenvalues of the Hamiltonian for a periodic potential form a band structure, and depending on the electrostatic interactions between the electrons and the lattice, energy gaps between the bands may occur, known as a band gap.

Since electrons are fermions, the Pauli exclusion principle forbids two electrons from occupying the same single-particle state, and electrons will therefore stack up, from the lowest band and upwards in energy. The highest energy occupied band in the ground state is known as the valence band, while the lowest, non-occupied band is known as the conduction band. If the valence band is partially filled, the electrons are free to move within a single band. The material will thus show metallic properties. However, if the band gap is large and the valence band is filled, the electrons will have difficulties moving around the band, and therefore the material behaves as an insulator. Finally, if the valence band is filled, but the band gap is small, electrons may be excited across the band gap and the material will exhibit many interesting and useful properties of a semiconductor.

In particular, a useful property of silicon is the excitation of electrons from the valence band to the conduction band when a charged particle passes through the material. Furthermore, the abscence of an electron in the valence band effectively behaves as a positively charged particle, known as a hole. This is known as an electron-hole pair and in silicon, on average $3.6\,\mathrm{eV}$ is required to excite such a pair. For a typical silicon sensor, $300\,\mu\mathrm{m}$ thick, Eq. (1) predicts a minimum energy of $0.12\,\mathrm{MeV}$ deposited, corresponding to $3.2 \cdot 10^4$ electron-hole pairs. Such a particle is known as a Minimum Ionizing Particle (MIP).

On the other hand, the intrinsic carrier concentration, n_i, of a semiconductor is

$$n_i = \sqrt{N_c N_v} \exp\Big(-\frac{E_g}{k_B T}\Big), \quad N_{c,v} = 2\Big(\frac{m_{e,h}^* k_B T}{2\pi\hbar^2} \Big)^{3/2}, \tag{3}$$

where $E_g = 1.1\,\mathrm{eV}$[] is the silicon band gap. At $T = 300\,\mathrm{K}$, the density of thermally excited electron-hole pairs, predicted by Eq. (3), is $4.4 \cdot 10^8$ for a typical silicon sensor area $A = 1\,\mathrm{cm}^2$. Thermally excited electrons and holes show up as noise in detector readings. Since this is many orders of magnitude larger than excited electron-hole pairs, pure silicon is not suitable as detector material, unless the thermally excited electrons and holes are removed.

2.3 PN-junction and reverse bias

The electron and hole concentrations in semiconductors may be modified by doping the material. Since silicon has 4 valence electrons, small amounts of material, such as phosphorus, with 5 valence electrons may be added in order

3

to increase the electron concentration, known as n-doped material. Similarly, addition of material with 3 valence electrons increase the hole concentration, called p-doped material.

In Fig. 1, an n-doped and p-doped block of silicon has been put together to form a PN-junction, which has properties suitable for a particle detector. At the junction, electrons from the N-side diffuses across to the P-side, leaving behind positive ions. Similarly, the holes on the P-side diffuses across and leaves behind negative ions. The ions create an electric field, with its direction from the N-side to the P-side, to oppose the diffusion of electrons and holes. The system will come to equilibrium when the number of electrons and holes in the junction has reduced until the diffusion and drift from the electric field cancel each other. The overall effect is to create a depleted zone at the junction, where all thermally excited electrons and holes have been diffused away.
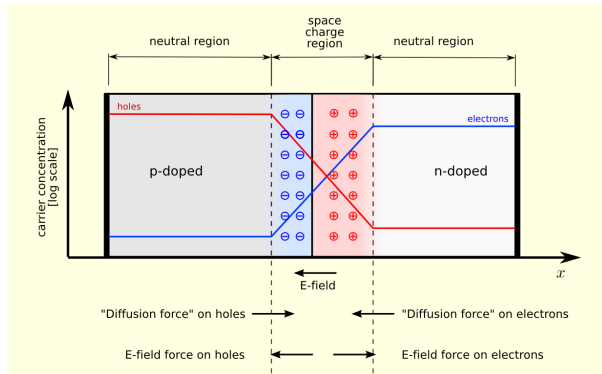
Figure 1: An overview of a PN-junction. Electrons and holes move, by diffusion, across the junction to free of charge carriers. The positive ions from the n-doped region and negative ions from the p-doped region create an electric field in the depletion zone.

When a charged particle passes through the depleted zone, electron-hole pairs are produced. However, since the concentration of thermal electrons and holes is much lower in the depletion zone, the excited electron-hole pairs may be read out as a signal.

However, a PN-junction as shown in Fig. 1 has a relatively small depletion zone, relative to the overall thickness of the silicon sensor. To extend the depletion zone, the PN-junction can be reverse biased, meaning a positive voltage is connected to the N-side and a negative

voltage to the P-side. The potential difference will increase the electric field and thus push the electrons and holes further away from the depletion zone. Thus, the depletion zone will extend, and for a sufficiently high voltage the full depth of the silicon sensor will be depleted.

The depletion zone is also known as the active part of the sensor. Since there is an electric field in this region, any exicted electron-hole pairs will drift in the fields, with electrons moving parallel to the field and holes moving antiparallel to the field. Therefore, signals from electron-hole pairs excited in the active region are much faster than the diffusion-driven signals from outside the depleted zone.

2.4 Analog readout and charge collection

When a charged particle excites electron-hole pairs in the depletion region, the signal is read out electronically. The reverse biased PN-junction effectively forms a capacitor, with negative charges on the P-side and positive charges on the N-side, separated by a depletion region that acts as an insulator. Therefore, the passage of a charge particle creates moving charges in the capacitor, or better known as a current.

There are many ways of converting this analogue signal into a useful, digital signal. Fig. 2 shows a short summary of the steps between energy deposit and digital signal readout. A real readout system may have many more steps, but Fig. 2 shows the essential steps. First, the incident particle deposits energy in the sensor, which results in a current. The preamplifier, which in a DMAPS is integrated in the pixel, integrates the current into a charge and converts this to a voltage drop. The pulse shaper changes the shape such that the pulse width is shorter, which reduces the overlap between successive pulses. The shaper also reduces some of the noise using a bandwidth filter. Finally, an analog to digital conversion, which is a discriminator that decides whether or not a signal counts as an event, results in the final output from the pixel.
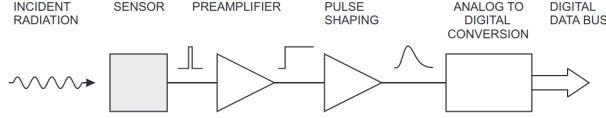
Figure 2: A schematic of how the energy deposited in a silicon detector is converted into a digital signal.

2.5   Signal formation in DMAPS

In this project, DMAPS sensors has been considered as a substitute for hybrid pixel detectors, which has been used in LHC detectors until now. Fig. 3 shows the general difference between a hybrid pixel, which is currently used in the ATLAS detector, and a monolithic pixel, which is studied in this report. The hybrid pixel, on the left, has the silicon sensor and the readout electronics separate, and connected through a bump-bond. This is a delicate and expensive process, and the bump-bonding process becomes increasingly harder as the pixel sizes decrease. Monolithic pixels solve these problems by having the readout electronics and the sensor in the same piece of silicon.
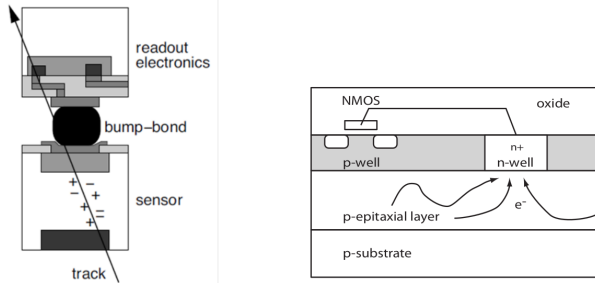
Figure 3: On the left is a hybrid pixel, where the sensor is separate from the readout electronics, connected through a bump-bond. On the right is a monolithic pixel, where both the sensor and the readout electronics is embedded in the same piece of silicon.

Fig. 4 shows a schematic of the ALICE Pixel Detector (ALPIDE), designed to replace the ALICE Inner Tracking System (ITS) during the long shutdown of LHC in 2019. It consists of a heavily p-doped silicon substrate that forms a good electrical contact with the backside, and a lightly doped epitaxial p-type silicon (p-epi) layer on top. The nwell on top conists of n-doped silicon. To reverse bias the p-doped substrate, a voltage V_{SUB} is applied to

the pwell on the top left corner. Since the region between the nwell on top and the top left pwell is only contains lightly doped p-type silicon, this region essentially becomes depleted when in contact the nwell and pwell. Thus, the nwell and top left pwell is separated by a depletion region, and this effectively becomes a PN-junction as described in Section 2.3. A small region around the nwell forms the active region, and any electrons from excited electron-hole pairs are collected by this nwell, known as the collection electrode.
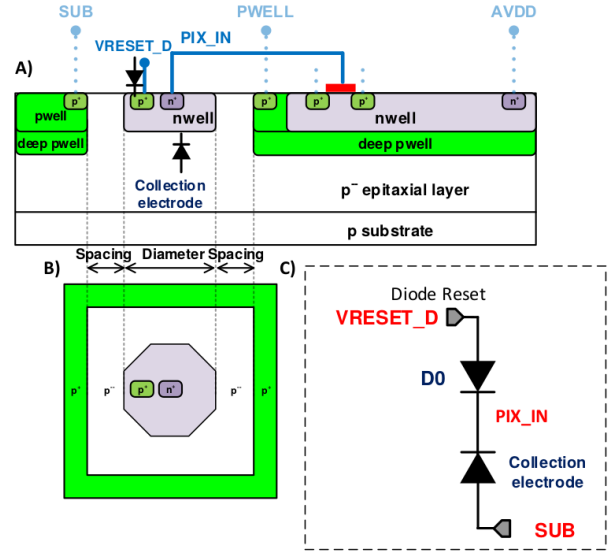
Figure 4: Schematic of the ALPIDE and its diode reset. The deep pwell separates the front end analogue electronics from the active region and the collection electrode.

The top right corner contains electronics circuitry for amplification of the signal. In particular, Fig. 4 shows two p-doped electrodes in an n-doped nwell, known as a P-type Metal Oxide Semiconductor (PMOS) transistor. NMOS transistors are also possible. The overall amplifier circuit contains multiple NMOS and PMOS transistors, implemented inside the deep pwell. The transistors are shielded by a deep pwell, such that none of the electron-hole pairs can drift into the circuitry.

In the bottom right of Fig. 4, an effective circuit of the nwell collection electrode and its connection with the substrate is shown. Here, the PN-junctions are shown as diodes. The bottom diode represents the junction between the collection electrode and the top left pwell, while the top diode represents the junction be-

tween the n$^+$ and p$^+$ implants inside the collection electrode. When a charged particle excites some electron-hole pairs with charge Q, the voltage in the region between the diodes is Q/C_c, where C_c is the capacitance of the collection electrode. By design, this voltage is inverted and is connected directly to the amplifier circuit inside the top right deep pwell region, as shown in blue.

Since the collection electrode is reverse biased, electrons are pushed by the electric field into the region between the diodes. Without the top diode, this charge would stay in this region indefinitely, which send a constant voltage $-Q/C_c$ into the amplifier. However, with the top diode connected to some voltage V_{RESET}, for a sufficiently large charge Q electrons will start flowing through the top diode, and hence the excess charge is emptied from the collection electrode. Since charges are emptied over a timescale of 1 ms, while the collection time is typically 10 ns, the input signal into the amplifier is typically a sharp step-function like drop in the voltage.

## 2.6 MALTA, Mini-MALTA and MALTA-Cz sensors

The MALTA sensor is based on the ALPIDE, but with a few modifications to increase the radiation hardness requires for the ATLAS detector. In particular, as shown in Fig. 5, the MALTA sensor contains an additional lighty doped n-type silicon layer between the p-epi layer and the nwell collection electrode and pwells on top. Furthermore, the bottom p-type substrate is now biased with a voltage V_{SUB}, independently of the bias voltage on the pwells on top, V_{PWELL}. The effect of this layer is that the depletion region fully extends horizontally and vertically, and the whole p-epi layer becomes depleted. This leads to a larger active region and a shorter drift time due to the increased electric field.
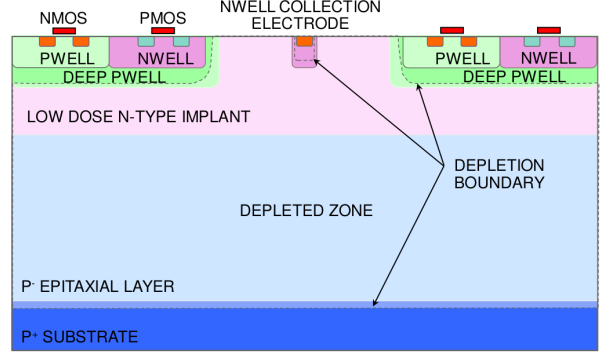
Figure 5: A side overview of the MALTA sensor. It differs from the ALPIDE by the extra lightly doped n-type silicon between the p-epi layer and the nwell and pwells. The substrate is also reverse biased.

After a signal has been amplified in the analogue amplifier on the MALTA pixel, the signal is further amplified in a digital circuit. The voltage drop is converted to a positive voltage pulse.

The MiniMALTA sensor is a further development of the MALTA sensor. The MALTA suffered from charge losses in the corners of the pixel due to the low electric fields, particularly after irradiation. The MiniMALTA therefore contains two new types of pixels, in addition to the original MALTA pixel. First, on the left in Fig. 6, is a pixel where the pwells have been made extra deep in the corners. Then, on the right in Fig. 6, the lightly doped n-type silicon has a gap in the corners.
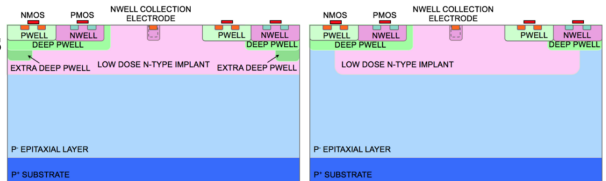
Figure 6: A sideview of two of the MiniMALTA pixels. On the left, the pwells have been modified to be extra deep in the corners, while of the right there is a gap in the lightly doped n-type silicon in the corners.

The MALTA-Cz is currently the most recent sensor. It is mostly the same as the MALTA sensor, but instead of a p-epi layer, a Czochralski process[] has been used to grow the crystal. This allows for a higher resistivity silicon with a deeper depletion region.

An important measurement in this project

has been to verify the improved performance of the modified pixels in the MiniMALTA, and to estimate the depletion depth of the MALTA-Cz.

3 Method

3.1 Radioactive sources: Fe-55 and Sr-90

To study the behaviour of the silicon sensors, two radioactive sources have been used: Fe-55 and Sr-90.

3.1.1 Fe-55

Fe-55[] decays via electron capture, $^{55}\text{Fe} + e- \rightarrow ^{55}\text{Mn}^+ + \nu_e$. The ^{55}Mn nucleus is in an excited state and emit X-rays. The probability $p_\alpha = 0.895$ of emitting an K_α X-ray with energy 5.90 keV and probability $1 - p_\alpha = 0.105$ of emitting an K_β X-ray with energy 6.49 keV. At this energy, the dominant interactions between the photons and the detector material is the photoelectric effect, with a small contribution of Compton scattering. Therefore, the photon is either completely absorbed or passes straight through.

When the photon is absorbed, it creates a small cloud of electron-hole pairs. If this cloud is fully contained in a pixel, the detector signal is proportional to the K_α or K_β energy, broadened by a Gaussian due to detector resolution. However, there is a finite probability p_{share} that the cloud is shared between two pixels. Therefore, we expect a uniform background of charge sharing signals at energies lower than K_α and K_β.

Let $G(E; E_0, \sigma_E)$ be a Gaussian distribution with mean E_0 and standard deviation σ_E. Let $U(E; E_{\text{max}})$ be a uniform distribution between $E = 0$ and $E = E_{\text{max}}$. Then a naiive Fe-55 spectrum would have the form

$$f(E) = p_\alpha \Big(p_{\text{share}} U(E; E_\alpha) + (1 - p_{\text{share}}) G(E; E_\alpha) \Big)$$

$$+ (1 - p_\alpha) \Big(p_{\text{share}} U(E; E_\beta) + (1 - p_{\text{share}}) G(E; E_\beta, \sigma_\beta) \Big) \qquad (4)$$

However, the Fe-55 spectrum also shows a small skewness in the Gaussians, weighted towards lower energies. It was proposed that this was due to charge that was not collected by the collection electrode, which appears as an energy loss. An empirical ansatz was made, where the energy loss is an exponential distribution, with a mean λE_α. Thus, the parameter λ represents the average fractional energy of the total K_α energy that is lost. To account for the energy loss, the exponential distribution is convoluted with Eq. (**??**). This distribution is fitted with the Fe-55 spectrum, with E_α, σ_α, E_β, σ_β, p_{alpha}, p_{share} and λ as free parameters. Thus, the exact position of E_α and E_β are extracted without interference from charge sharing or energy loss.

3.1.2 Sr-90

Sr-90 decays via β^- decay, $^{90}\text{Sr} \rightarrow ^{90}\text{Y}^+ + e^- + \bar{\nu}_e$, and the average e^- energy is $E_e = 196$ keV. The energy deposited follows Eq. (1), and the spectrum is approximately a Landau distribution. It is not an exact Landau distribution because of the spread in e^- energy. Although an exact, analytic expression for a Landau distribution does not exist, a parameterization is available in the Python module PyLandau[], with the position E_p of the most probable energy, the width η of the peak and the normalization A as free parameters. By fitting this to the spectrum, an estimation of E_p is obtained.

In Silicon, the average energy of each electron-hole pair is 3.6 eV[]. Furthermore, the most probable energy deposited in Silicon is 76 µm^{-1}. Thus, by measuring E_p, the thickness of the depletion depth is obtained.

3.2 Data taking using an oscilloscope

The experimental setup for the MiniMALTA is shown in Fig. 7. The upper power supply supplies the analogue and digital amplifiers. The bottom power supply supplies the reverse bias to the substrate and pwell. The signals are recorded using an oscilloscope. Four probes are connected to four different monitoring pixels. The sensor itself if placed in a black box to shield the sensor from the daylight and from the lamps. Finally, a radioactive source is placed on top of the sensor and the black box is sealed with a lid. The Fe-55 is small enough to be placed directly on the board, while the Sr-90 source has a separate support.
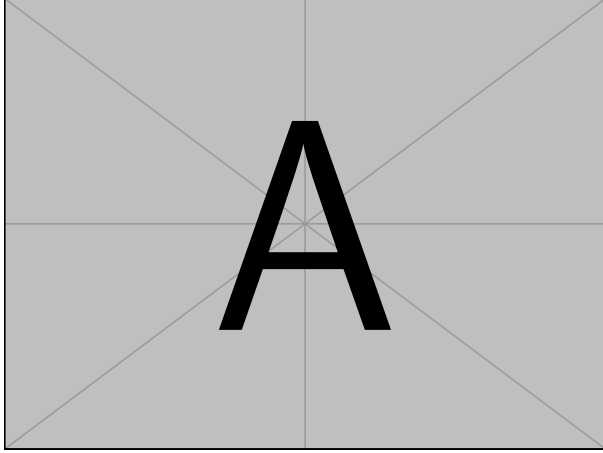
Figure 7: Setup of the experimental equipment. (1) Power supplies. (2) Oscilloscope. (3) Probes connected to the monitoring pixels. (4) Black box to shield the sensor from background light. (5) MiniMALTA sensor. (6) Fe-55 radioactive source. (7) Sr-90 radioactive source.

After the black box was sealed, the lamps in the room were turned on and off to make sure that there was no change in the output signal baseline. A potential gap in the box that would cause a constant voltage change in the baseline was not observed. Then the oscilloscope trigger was configured to record all three channels when the voltage of any channel crosses a threshold. The threshold is chosen by hand for each channel separately such that most of the electronic noise does not trigger.

For the MALTA and MALTA-Cz, the setup is almost identical. However, since the monitoring pixels contain a digital amplifier, an Field Programmable Gate Array (FPGA) was also connected directly to the board. The FPGA was programmed using Vivado with code developed by CERN[] that configures all necessary settings for the digital amplifier. A photo of the FPGA is shown in Appendix **??**. Also, only 3 monitoring pixels have been used because the MALTA-Cz was missing a wire bond in the fourth pixel.

All sensors required a voltage of $1.8\,\text{V}$ to power the analogue and digital amplifier. The reverse bias voltage for MiniMALTA were $V_{\text{SUB}} = V_{\text{PWELL}} = 1.5\,\text{V}$. For MALTA the corresponding values are $V_{\text{SUB}} = 10\,\text{V}$ and $V_t extPWELL = 6\,\text{V}$, while MALTA-Cz has $V_{\text{SUB}} = 35\,\text{V}$ and $V_t extPWELL = 6\,\text{V}$.

3.3 Fitting signals

3.4 MiniMALTA

The MiniMALTA had monitoring pixels where the output from the analogue amplifier could be read out directly without the digital circuit. Thus, the signal had the form of a voltage drop, modelled as an exponential decay. A curve of the form

$$f(t) = \begin{cases} A, & t < t_0 \\ C \exp\left(-\frac{t}{T}\right) + (A - C), & t > t_0, \end{cases}$$

where A, C and t_0 are free parameters. The parameter C is the amplitude of the signal.

3.5 MALTA and MALTA-Cz

The MALTA and MALTA-Cz only has outputs after the signal has been through a digital amplifier, and the signal is therefore a pulse. For small signals, the pulse seem to have an exponential voltage jump, which is similar to the voltage of of the MiniMALTA, but positive. The difference is that the pulse quickly drops back to the baseline, with some exponential decay. However, for larger signals, the pulse becomes clipped, such the top of the pulse has a flat plateau instead of a peak. It is parameterized in the form

$$f(t) = \begin{cases} A, & t < t_0 \\ A + B * \left(\tanh\left(\frac{t-\tau}{T_1}\right) - \frac{1}{2}\tanh\left(\frac{t-t_1}{T_2}\right) - \frac{1}{2}\right), & t > t_0, \end{cases}$$

where

$$\tau = T_1 \operatorname{arctanh}\left(\frac{1}{2}\left(\tanh\left(\frac{t_1}{T_2}\right) - 1\right)\right).$$

After fitting this to each pulse, the baseline A is determined accurately. However, the height of the pulse is no longer an accurate measure of the energy deposited by the e^- because of the clipping of the pulse. An alternative way to measure the energy is to measure the pulse length at some threshold height above the baseline. Since the pulse shape is already stored as a list, the pulse length is simply measured by counting the number of list elements with values greater than the threshold height.

To reduce the number of noise hits, a point is only counted if, in addition, the 15 points on each side of the point considered are also above the height threshold.

4 Analysis

4.1 MiniMALTA

4.1.1 Energy calibration with Fe-55

The empirical model described in Section 3.1.1 was used to fit a histogram of amplitudes from Fe-55 signals in the MiniMALTA. Fig. 8 shows the Fe-55 spectrum for a standard MiniMALTA pixel. The four pixels studied in this project all show similar behaviour.
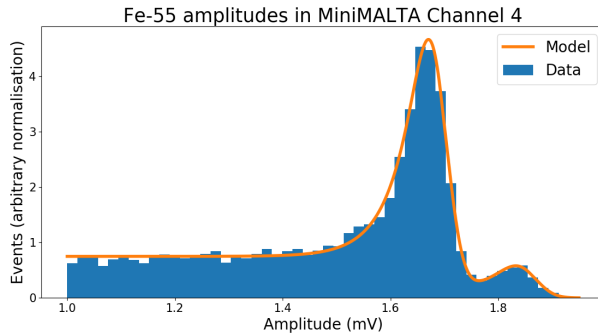
Figure 8: A Fe-55 spectrum from a standard pixel in the MiniMALTA. The horizontal axis is the amplitude, measured in mV, while the vertical axis is the number of events, with arbitrary normalisation. In blue is the experimental data, while the orange curve is a fit using the empirical model from Section 3.1.1.

Table 1 shows the best fit parameters E_α, E_β and p_α, in addition to the ratio E_β/E_α. The expected fraction of K_α signals is 0.88[], which is within errors for all pixels. Similarly, we expect $E_\beta/E_\alpha = 1.1$[], in good agreement with the data.

**Table 1:** Best fit parameters for the MiniMALTA response to Fe-55 signals.

| Channel	E_α(mV)	E_β(mV)	p_α	E_β/E_α
1	1.6831 ± 0.0015	1.849 ± 0.008	0.881 ± 0.013	1.098 ± 0.005
2	1.7004 ± 0.0013	1.865 ± 0.004	0.882 ± 0.008	1.0968 ± 0.0025
3	2.8219 ± 0.0022	3.104 ± 0.007	0.890 ± 0.010	1.1000 ± 0.0026
4	1.6979 ± 0.0009	1.863 ± 0.005	0.877 ± 0.009	1.097 ± 0.007

These cross checks confirm that the obtained values of E_α and E_β are indeed accurate.

4.1.2 Measurement of the depletion region with Sr-90

With an accurate value of E_α, a conversion between the amplitude in mV to eV is available, such that the depletion depth of the MiniMALTA may be measured using Sr-90. Figs. 9-12 show histograms of Sr-90 signals using the MiniMALTA. In blue is the experimental data, while in red is a best fit Landau distribution. The horizontal axis is the amplitude in mV, while the vertical axis is the number of events, with arbitrary normalisation.
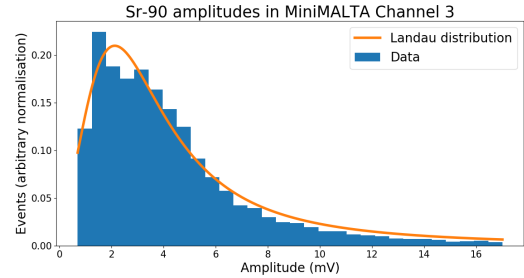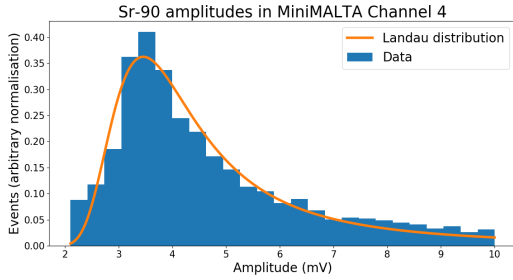

Figure 9: A Sr-90 spectrum from pixel 1 in the MiniMALTA. This particular pixel is modified with an extra deep pwell in the corners.
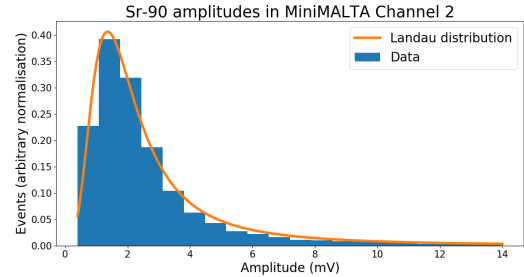
Figure 10: A Sr-90 spectrum from pixel 2 in the MiniMALTA. This particular pixel is modified with a gap in the lightly doped n-type silicon in the corners.
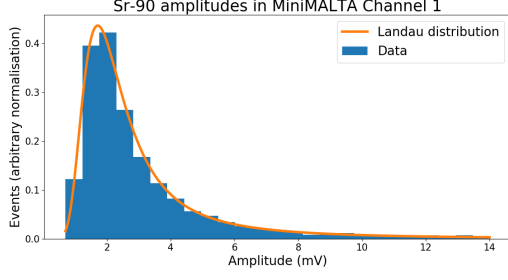
Figure 11: A Sr-90 spectrum from pixel 3 in the MiniMALTA. This particular pixel is modified an nwell in the region where the transistors for the analogue amplifier is usually located.

Figure 12: A Sr-90 spectrum from a pixel 4 in the MiniMALTA. This particular pixel is identical to the ones found on the MALTA sensor.

Clearly, Figs. 9 and 10 show an excellent fit with a Landau diststribution. Fig. 12 shows a poor fit because some of the signals have been pushed down in energy. This could be explained by charges being lost in the corners of the pixel. Furthermore, previous studies have shown that large active areas lead to negative effects in charge collection, and this pixel has an active area where the transistors for the analogue amplifier is usually located. In pixel 4, this region has been filled with an nwell, and Fig. 11 shows some improvements to the charge collection, although not perfect. Thus, it is clear that the special corner implants in pixel 1 and 2 improve the charge collection, giving much better agreement with a Landau distribution of energy deposition in the silicon.

Table 2 shows the estimated depletion depth d for the MiniMALTA pixels. The poor fit in Figs. 11 and 12 is reflected in the large errors in the depletion depths for pixel 3 and 4. However, all four pixels show good agreement with the designed

Table 2: Estimated depletion depths in the Mini-MALTA pixels, using Sr-90 for measuring the most probably energy deposit and Fe-55 for energy calibration.

Pixel	1	2	3	4
d(µm)	22 ± 3	17 ± 3	27 ± 14	26 ± 14

4.2 MALTA and MALTA-Cz

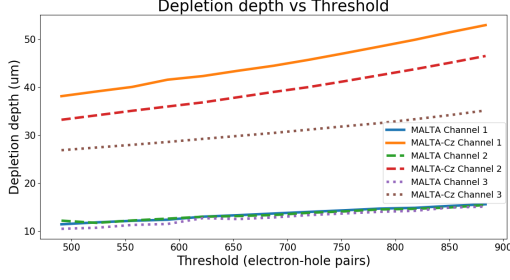### 4.2.1 Absolute measurement of the depletion depth

In principle the calculation of the depletion depth of MALTA and MALTA-Cz is identical to that of MiniMALTA. The response of the MALTA and MALTA-Cz to Fe-55 is almost identical as the MiniMALTA. From the fitted value of E_α, the calibration between pulse length and energy is obtained. Together with the most probable energy deposited, which is obtained by fitting a Landau distribution to the Sr-90 signals, a depletion depth is obtained.

An example of a fitted Landau distribution is shown in Fig. 13.
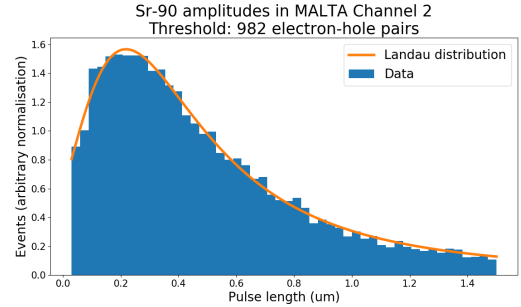
Figure 13: The distribution of pulse lengths from Sr-90 signals in MALTA, together with a Landau distribution fitted to the data.

However, an issue with using the pulse length as a measure of energy deposition is the choice of height threshold. Fig. 14 shows the depletion depth calculated, as a function of height threshold. The height threshold is expressed in terms of the number of electron-hole pairs. Since each electron-hole pair require 3.6 eV on average, a K_α X-ray will create 1640 electron-hole pairs[], and the height thresholds have been chosen to be a fraction between 0.30 to 0.54 of the K_α energy of each pixel.

Figure 14: The depletion depth of MALTA and MALTA-Cz as a function of the height threshold for pulse length measurement.

Due to the different voltage gain in each probe, the same probes used measure Fe-55 signals are used for the same pixels when measuring the Sr-90 signals. The E_α calculated from the Fe-55 signals for each pixel determines the energy scale for each pixel in terms of pulse lengths, here expressed as the number of electron-hole pairs.

Fig. 14 clearly indicates a strong dependence on the height threshold chosen, especially for MALTA-Cz. This is since Fe-55 only provide a calibration between pulse length to energy for a single energy, E_α. If the signal pulse had had a perfect triangular shape, the choice of height threshold would have made no difference. However, the measured pulses have a clear bend in the tail of the pulse. Without an accurate gain calibration between pulse length and energy, there is no way to tell which heigh threshold that will give an accurate estimate of the depletion depth. MALTA-Cz suffers more from these issues because the most probable energy deposited by Sr-90 electrons have a much larger energy, relative to the K_α X-rays. Thus, The MALTA-Cz curves in Fig. 14 show a stronger dependence on the threshold.

4.3 Relative measurement of the depletion depth

To obtain a more reliable measurement of the depletion depth of MALTA-Cz, a relative measurement could be estimated instead. Current measurements of the MALTA depletion depths range between $20\,\mu\text{m}$ to $25\,\mu\text{m}$. Therefore, the depletion depth of MALTA-Cz could be measured relative to this.

Since the pulse shapes are more or less iden-

tical for MALTA and MALTA-Cz, we would expect the calibration errors to cancel if the ratio between the depletion depth for MALTA and MALTA-Cz is taken, for a fixed height threshold. Fig. 15 shows the depletion depth of MALTA-Cz, relative to that of MALTA. Clearly, within errors this is constant as a function of height threshold.
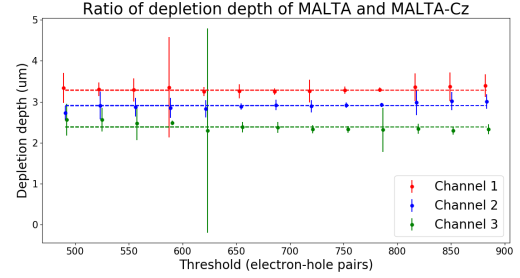
Figure 15: The depletion depth ratio between MALTA and MALTA-Cz as a function of the height threshold for pulse length measurement.

The final depletion depth can be found by fitting a constant line, shown as dashed in Fig. 15. We observe that there is a difference across the pixels. While a spread in depletion depths of a few µm across neighbouring pixels is expected, the observed spread in Fig. 14 and Fig. 15 are slightly larger than expected for MALTA-Cz. Table 3 shows the fitted values, together with a statistical error.

Table 3: Estimated depletion depths of MALTA-Cz, relative to MALTA.

Pixel	1	2	3
$d_{\text{MALTA}}/d_{\text{MALTA-Cz}}$	3.28 ± 0.04	2.90 ± 0.03	2.39 ± 0.03

Whether or not the spread in depletion depth across the pixels is a calibration issue or a property of the sensor is difficult to tell. For this report, I will treat the spread as a systematic calibration error. Thus, the final depletion depth ratio is estimated to be $2.86 \pm 0.03 \pm 0.4$, where the first error is the statistical error and the second error is the systematic calibration error, calculated from the standard deviation of Table 3.

5   Conclusion

A measurement of the depletion depths has been performed with the MiniMALTA, MALTA and MALTA-Cz sensors using Fe-55 and Sr-90 radioactive sources.

The MiniMALTA depletion depth should be in the range $20\,\mu m$ to $25\,\mu m$, and the observed values agreed within errors, although on the lower side. This could indicate that the pixel was not fully depleted.

The measurement of the MALTA-Cz depletion depth is the first of its kind, and it is an important piece of data for the development of DMAPS sensors for use in the ATLAS ITK. This could significantly reduce the production costs and material budget of future tracker detectors in ATLAS, and the use of DMAPS in future HEP detectors is a great milestone. The final depletion depth was $2.86 \pm 0.03 \pm 0.4$, relative to that of MALTA. The dominant errors were due to systematic calibration errors when measuring the energy deposited using the pulse length instead of pulse height.

A next step is to perform the same measurements for irradiated samples of MALTA-Cz. In addition, with a wider range of X-ray sources with different K_α energies, a better calibration between pulse length and energy could be obtained in order to improve the current and future measurements of the depletion depth.

References

[1] M. Dyndal et al. Mini-MALTA: radiation hard pixel designs for small-electrode monolithic CMOS sensors for the High Luminosity LHC. *JINST*, 15(02):P02005.